Nematic spin fluid in the tetragonal phase of BaFe_{2}As_{2}

L. W. Harriger, H. Q. Luo, M. S. Liu, C. Frost, J. P. Hu, M. R. Norman, and Pengcheng Dai

Phys. Rev. B **84**, 054544 — Published 24 August 2011

DOI: 10.1103/PhysRevB.84.054544

Nematic spin fluid in the tetragonal phase of $BaFe_2As_2$

L. W. Harriger [1], H. Q. Luo[2], M. S. Liu[1], T. G. Perring[3], C. Frost[3], J. P. Hu[4,2], M. R. Norman[5], and Pengcheng Dai[1,2,6*]

[1]Department of Physics and Astronomy, The University of Tennessee, Knoxville, Tennessee 37996-1200, USA

[2]Beijing National Laboratory for Condensed Matter Physics, Institute of Physics, Chinese Academy of Sciences, Beijing 100190, China

[3]ISIS Facility, Rutherford Appleton Laboratory, Chilton, Didcot, Oxfordshire OX11 0QX, UK

[4]Department of Physics, Purdue University, West Lafayette, Indiana 47907, USA

[5]Materials Science Division, Argonne National Laboratory, Argonne, Illinois 60439, USA

[6]Neutron Scattering Science Division, Oak Ridge National Laboratory, Oak Ridge, Tennessee 37831, USA

[*]**pdai@utk.edu**

Abstract:

We use inelastic neutron scattering to study spin waves below and above T_N in iron-arsenide $BaFe_2As_2$. In the low-temperature orthorhombic phase, we find highly anisotropic spin waves with a large damping along the antiferromagnetic (AF) *a*-axis direction. On warming the system to the paramagnetic tetragonal phase, the low-energy spin waves evolve into quasi-elastic excitations, while the anisotropic spin excitations near the zone boundary persist. These results strongly suggest the

presence of a spin nematic fluid in the tetragonal phase of $BaFe_2As_2$, which may cause the electronic and orbital anisotropy observed in these materials.

I. Introduction

Magnetic interactions are generally believed to play a key role in mediating electron pairing for superconductivity in iron arsenides[1-4], yet their character is only partially understood[5-8]. Correlated electron materials can exhibit a variety of complex phases that control the electronic and transport properties of these materials. For example, an electronic nematic phase, where the C_4 symmetry of the paramagnetic phase is spontaneously broken, has been postulated as the source of the pseudogap behavior observed in copper oxide superconductors[18-20]. Furthermore, the tetragonal to orthorhombic structural phase transition preceding or coincidental with the static AF order (with spin structure shown in Fig. 1a) in the parent compounds of iron pnictide superconductors[5,6] has been suggested to arise from a spin nematic phase[11,12]. Although neutron scattering[7], scanning tunneling microscopy[13], transport[14,15], optical conductivity[16], and angle resolved photoemission[17] experiments have provided evidence for electronic anisotropy, these measurements are carried out either in the low temperature orthorhombic (LTO) phase[7,13], where the crystal lattice structure has already broken C_4 symmetry[5,6], or in the tetragonal phase under uniaxial pressure that also breaks this symmetry[14-17]. Therefore, it is unclear whether electronic anisotropy can exist in a truly tetragonal phase without an external driving field. A decisive answer to this question will not only reveal the microscopic origin of the lattice and magnetic transitions

in iron arsenides, but will also determine the importance of electron correlations and orbital degrees of freedom in these materials[18-24].

In this article, we use inelastic neutron scattering to demonstrate the presence of a large in-plane spin anisotropy above T_N in the unstressed tetragonal phase of $BaFe_2As_2$. In the LTO phase, we find highly anisotropic spin waves in $BaFe_2As_2$ with a large damping along the AF *a*-axis direction. On warming the system to the paramagnetic tetragonal phase, the low-energy spin waves evolve into quasi-elastic excitations, while the anisotropic spin excitations near the zone boundary persist. These results strongly suggest that the spin nematicity in $BaFe_2As_2$ is the source of the electronic and orbital anisotropy observed above T_N by other probes[14-17].

Using inelastic neutron scattering, we first show that the spin waves of $BaFe_2As_2$ ($T_N \approx 138$ K, [6]) in the LTO phase imply highly anisotropic magnetic exchange couplings similar to those seen in $CaFe_2As_2$ [7] and these spin waves are strongly damped along the AF *a*-axis direction (Figs. 1c-f). Upon warming the material to the tetragonal paramagnetic phase[5,6], the anisotropic high-energy (>100 meV) spin excitations near the zone boundary persist, while the low-energy spin waves near the zone center evolve into paramagnetic spin excitations (Figs. 2-4). These results provide compelling evidence for a nematic spin fluid that breaks the tetragonal C_4 symmetry of the underlying crystalline lattice and spontaneously forms without the need for uniaxial pressure. Moreover, we suggest that this spin anisotropy causes a splitting of the d_{xz} and d_{yz} orbital bands in the tetragonal phase[18-24] , which in turn leads to the orthorhombic lattice distortion and electronic anisotropy.

II. Experimental Results

Previous powder[25] and single crystal[26] measurements for excitation energies below 100 meV revealed that the spin waves in $BaFe_2As_2$ are three-dimensional and centered at the AF wave vector $\boldsymbol{Q}$ = (1,0, L = 1, 3, 5, …) in reciprocal lattice units (rlu). For $CaFe_2As_2$, spin waves form well-defined ellipses centered around the AF $\boldsymbol{Q}$ throughout the Brillouin zone[7]. Our inelastic neutron scattering experiments were carried out on the MAPS time-of-flight chopper spectrometer at the Rutherford-Appleton Laboratory, Didcot, UK. We co-aligned ~25 grams of single crystals of $BaFe_2As_2$ grown by self-flux using the HB-1 triple axis spectrometer at the High Flux Isotope Reactor at Oak Ridge National Laboratory. The incident beam energies were E_i = 80, 250, 450, 600 meV, and with k_i parallel to the c-axis. Spin wave intensities were normalized to absolute units using a vanadium standard (with 30% error). We define the wave vector $\boldsymbol{Q}$ at (q_x,q_y,q_z) as $(H, K, L) = (q_x\, a/2\pi\,, q_y\, b/2\pi\,, q_z\, c/2\pi)$ in rlu, where a = 5.62, b = 5.570, and c = 12.97 Å are the orthorhombic cell lattice parameters at 10 K [6].

Figs. 2a-e show two-dimensional constant-energy (E) images of spin-wave excitations of $BaFe_2As_2$ in the (H, K) scattering plane for several Brillouin zones at L = 1, 3, 5, 7. For energy transfers of E = 26 ± 10 (Fig. 2a) and 81 ± 10 meV (Fig. 2b), spin waves are still peaked at $\boldsymbol{Q}$ = (1,0) in the center of the Brillouin zone shown as dashed square boxes. As the energy increases to E = 113 ± 10 (Fig. 2c), 157 ± 10 (Fig. 2d), and 214 ± 15 meV (Fig. 2e), spin waves no longer form ellipses centered around $\boldsymbol{Q}$ = (1,0). Instead, they start to split along the K-direction and form an anisotropic and asymmetric

ring around $\boldsymbol{Q}$ = (±1, ±1), in stark contrast with the spin waves at similar energies seen in $CaFe_2As_2$ (Figs. 1e-1i of [7]).

To understand the low-temperature spin waves in $BaFe_2As_2$, we cut through the two-dimensional images similar to Fig. 2 for incident beam wave vectors (k_i) aligned along the *c*-axis. Figs. 1e and 1f show spin wave dispersions along the (1,*K*) and (*H*,0) directions, respectively. Fig. 2f shows the background subtracted scattering for the E_i = 450 meV data projected in the wave vector ($\boldsymbol{Q}$ = [1,*K*]) and energy space. Similar to spin waves in $CaFe_2As_2$ [7], we can see three clear plumes of scattering arising from the in-plane AF zone centers $\boldsymbol{Q}$ = (1,-2), (1,0), and (1,2) extending up to about 200 meV. We have attempted but failed to fit the entire spin wave spectra in Fig. 2 using a Heisenberg Hamiltonian consisting of effective in-plane nearest-neighbors (Fig. 1a, J_{1a} and J_{1b}), next-nearest-neighbor (Fig. 1a, J_2), and out-of-plane (J_c) exchange interactions with an isotropic spin wave damping parameter Γ(black curves in Fig. 1c and appendix)[7]. However, allowing for an anisotropic spin wave damping parameter Γ(Fig. 1d) produces an energy dependence of the spin wave profiles (color plots in Fig. 1c) that is qualitatively similar to what we observe (Figs. 2a-2e). Using this $\boldsymbol{Q}$-dependent damping $\Gamma(H, K)$ (see appendix), we were able to fit the entire measured spin wave excitation spectra in absolute units by convolving the neutron scattering spin-wave cross section with the instrument resolution[7]. The effect of twin domains is taken into account by *a*/*b* averaging (see supplementary material). Consistent with earlier results on $CaFe_2As_2$ (Ref. 7), we find that the Heisenberg Hamiltonian with $SJ_{1a} \approx SJ_{1b} \approx \frac{1}{2}SJ_2$ fails to describe the zone boundary data (Fig. 1e). Our best fits to both the low-energy and zone

boundary spin waves are shown as solid lines in Fig. 1e and color plots in Figs. 2g-l with $SJ_{1a} = 59.2 \pm 2.0$, $SJ_{1b} = -9.2 \pm 1.2$, $SJ_2 = 13.6 \pm 1.0$, $SJ_c = 1.8 \pm 0.3$ meV.

Comparing the above fitted results for $BaFe_2As_2$ with those for $CaFe_2As_2$ [7], we see that while the in-plane effective magnetic exchanges (SJ_{1a}, SJ_{1b}) are very similar in these two materials, there is ~30% reduction in SJ_2 when Ca is replaced by the larger Ba and the *c*-axis exchange coupling is reduced considerably (from $SJ_c = 5.3 \pm 1.3$ meV for $CaFe_2As_2$). In addition, while one can see clear spin wave ellipses centered around $\boldsymbol{Q}$ = (1,0) in $CaFe_2As_2$ at all energies[7], spin waves in $BaFe_2As_2$ are heavily damped along the *a*-axis direction and become hardly observable for energies above 100 meV. These results are consistent with random phase approximation calculations (see appendix)[27].

Having demonstrated that $BaFe_2As_2$ exhibits a large spin anisotropy in the LTO phase, it is important to determine if this spin anisotropy also exists in the high-temperature tetragonal phase, where the underlying crystal lattice structure has C_4 rotational symmetry. In a recent work on $CaFe_2As_2$, spin excitations in the paramagnetic tetragonal phase were found to have a similar spatial line-shape as those of the low-temperature spin waves below 60 meV [28]. These anisotropic short-range AF fluctuations can be interpreted as frustrated paramagnetic scattering[28]. If the observed large anisotropy of SJ_{1a} and SJ_{1b} for $BaFe_2As_2$ (Figs. 1 and 2) and $CaFe_2As_2$ [7] in the LTO phase becomes isotropic ($SJ_{1a} = SJ_{1b}$) in the paramagnetic tetragonal phase, one would expect a huge softening of the zone boundary spin waves upon entering into the tetragonal phase (see dotted lines in Fig. 1e), which we do not observe. Figure 3 summarizes the temperature dependence of the spin wave excitations at temperatures of $0.05T_N$, $0.93T_N$, and $1.09T_N$. For spin wave energies of $E = 50 \pm 10, 75 \pm 10$ meV, we

confirm the earlier result[28] on $CaFe_2As_2$ and find that spin excitations above T_N are weaker and broader than the spin waves below T_N (Figs. 3a-f). However, spin waves at energies of $E = 125 \pm 10, 150 \pm 10$ meV have virtually no temperature dependence of their intensity and line shape across the AF orthorhombic to paramagnetic tetragonal phase transition (Figs. 3g-l). Therefore, spin excitations near the zone boundary do not exhibit huge softening in the paramagnetic state, which implies that the large in-plane exchange anisotropy persists above T_N without spin frustration.

To test whether the observed scattering above T_N indeed arises from localized spin excitations similar to the spin waves below T_N and not from paramagnetic scattering centered at zero energy, we carried out energy cuts of the spin excitations at different positions of the dispersion as shown in the inset of Fig. 4a. Near the Brillouin zone center at $\boldsymbol{Q}$ = (1,0.05) and (1,0.02), well-defined spin waves are observed at E = 32, and 50 meV, respectively (blue diamonds in Figs. 4a and 4b), in the AF ordered state. Upon warming to the paramagnetic tetragonal state $T = 1.09T_N$, the spin wave peaks disappear and spin excitations become purely paramagnetic with their highest intensity centered at zero energy (red circles in Figs. 4a and 4b). Moving closer to the zone boundary at $\boldsymbol{Q}$ = (1,0.35), the spin wave peaks at 90 meV are virtually unchanged on warming from $0.05T_N$ to $0.93T_N$ and decrease only slightly in intensity at $1.09T_N$ (Fig. 4c). At $\boldsymbol{Q}$ = (1,0.5), spin wave peaks at E = 125 meV are temperature independent below and above T_N (Fig. 4d). Figs. 4e and 4f show the $\boldsymbol{Q}$-dependence of the magnetic scattering at $E = 19 \pm 5$ and 128 ± 5 meV, respectively. Consistent with Fig. 3, the spin waves at low energies become broad paramagnetic spin excitations above T_N, while they stay unchanged at high energies near the zone boundary (Figs. 4e and 4f). The energy

dependence of the dynamic spin-spin correlation lengths below and above T_N in Fig. 4g suggests that short-range spin excitations at energies above ~100 meV are not sensitive to the orthorhombic to tetragonal phase transition and do not reflect the C_4 symmetry. The effective magnetic exchange couplings SJ_{1a} and SJ_{1b} in spin clusters of sizes $\xi = 15 \pm 3$ Å must be anisotropic, and therefore locally break the C_4 tetragonal symmetry.

III. Discussions and Conclusions

We have discovered that the spin waves in $BaFe_2As_2$ are highly anisotropic with a large damping along the metallic AF a-axis direction in the LTO phase (Figs. 1 and 2). On warming to the paramagnetic tetragonal phase, the low-energy spin waves near the zone center evolve into paramagnetic scattering, while the anisotropy of the high-energy spin excitations near the zone boundary persists (Figs. 3 and 4). This means that the short-range effective magnetic exchange couplings in $BaFe_2As_2$ are anisotropic and unchanged across T_N, consistent with a nematic spin fluid that breaks the C_4 symmetry of the tetragonal phase. In previous observations of electronic nematic phases in different materials, there is usually a symmetry breaking field present, such as an external magnetic field, uniaxial pressure, or an orthorhombic crystalline lattice[12-17], which is not the case here. The observation of a short-range spin nematic phase in the tetragonal state of $BaFe_2As_2$ reveals the presence of strong spin-orbital coupling at temperatures above T_N [17-24,29].

The persistence of spin anisotropy in the paramagnetic phase has obvious implications for the nature of the magnetism in pnictides, which in turn has potentially

profound implications for the origin of superconductivity. Anisotropy in the resistivity has been seen to persist for Co doped $BaFe_2As_2$ samples into the region of the phase diagram where superconductivity exists[14]. Moreover, the existence of a spin resonance in the superconducting state of Ni doped $BaFe_2As_2$, which is a doublet rather than a triplet, is also consistent with local spin nematicity[30]. Since the spin excitations at short length scales are intrinsically nematic in the paramagnetic tetragonal phase, the AF phase transition and lattice distortion are likely induced by nematic spin fluctuations. On the other hand, if orbital ordering were driving the spin nematicity, one would expect a gradual change of spin anisotropy across T_N depending on the strength of spin-orbital coupling, contrary to our observations. Since the spin nematicity leads to an enormous anisotropy in the near-neighbor exchange couplings, this could have a profound impact on the nature of the superconducting electron pairing interaction. In that connection, it is interesting to note that there appears to be an anti-correlation between the spin nematicity and the superconducting gap anisotropy, in that the latter appears to switch from *s*-wave-like to *d*-wave-like[31] at a doping where the spin nematicity disappears in the transport measurements[14].

After finishing the present work, we became aware of a related neutron scattering work on $SrFe_2As_2$, where strong magnetic anisotropy was reported in the paramagnetic state[32]. Although these authors prefer to use itinerant approach to interpret their data, the central conclusion of an electronic anisotropy in the paramagnetic phase is consistent with results present in our paper.

IV. **Acknowledgements**

We thank E. Kaneshita and T. Tohyama for helpful discussions and providing numerical calculations for Fig. A8. The neutron scattering work at UT is supported by the US NSF-OISE-0968226 and NSF-DMR-1063866. The single crystal growth efforts at UT are supported by DOE BES DE-FG-02-05ER46202. This work is also supported by the US DOE Division of Scientific User Facilities. Work at ANL is supported by the US DOE under Contract No. DE-AC02-06CH11357. The single crystal growth and neutron scattering work at IOP is supported by the Chinese Academy of Sciences, and by 973 program (2010CB833102 and 2010CB923002).

Appendix

To understand the spin wave data as shown in Figs. 1-4, we consider a Heisenberg Hamiltonian consisting of effective in-plane nearest-neighbors (Fig. 1a, J_{1a} and J_{1b}), next-nearest-neighbor (Fig. 1a, J_2), and out-of-plane (J_c) exchange interactions. The dispersion relations are given by: $E(q) = \sqrt{A_q^2 - B_q^2}$, where $A_q = 2S[J_{1b}(\cos(\pi K) - 1) + J_{1a} + J_c + 2J_2 + J_s]$,

$B_q = 2S[J_{1a}\cos(\pi H) + 2J_2\cos(\pi H)\cos(\pi K) + J_c\cos(\pi L)]$, J_s is the single ion anisotropy constant, and q is the reduced wave vector away from the AF zone center. The neutron scattering cross section can be written as:

$\frac{d^2\sigma}{d\Omega dE} = \frac{k_f}{k_i}\left(\frac{\gamma r_0}{2}\right)^2 g^2 f^2(Q) e^{-2W} \sum_{\alpha\beta}\left(\delta_{\alpha\beta} - Q_\alpha Q_\beta\right) S^{\alpha\beta}(Q,E)$, where

$(\gamma r_0/2)^2 = 72.65$ mb/sr, g is the g-factor (≈ 2), $f(Q)$ is the magnetic form factor of iron

Fe^{2+}, e^{-2W} is the Debye-Waller factor (≈ 1 at 10 K), Q_α is the α component of a unit vector in the direction of Q, $S^{\alpha\beta}(Q,E)$ is the response function that describes the $\alpha\beta$ spin-spin correlations, and k_i and k_f are incident and final wave vectors, respectively. Assuming that only the transverse correlations contribute to the spin-wave cross section and finite excitation lifetimes can be described by a damped simple harmonic oscillator with inverse lifetime Γ, we have

$$S^{yy}(Q,E) = S^{zz}(Q,E) = S_{eff}\frac{(A_q - B_q)}{E_0\left(1-e^{-E/k_BT}\right)}\frac{4}{\pi}\frac{\Gamma E E_0}{\left(E^2-E_0^2\right)^2+4(\Gamma E)^2},$$

where k_B is the Boltzmann constant, E_0 is the spin-wave energy, and S_{eff} is the effective spin. Assuming isotropic spin wave inverse lifetime Γ, we were unable to find any effective exchange couplings that will describe the entire spin wave spectra as shown in Fig. 2a-f. To resolve this problem, we have used an anisotropic spin wave damping Γ assuming $\Gamma(H,K) = \Gamma_0 + \Gamma_1 E + A(\cos(\frac{\pi H}{2}))^2 + B(\cos(\frac{\pi K}{2}))^2$, where A and B are parameters controlling the magnitude of the spin wave damping. For the best fit to the spin wave data, we have $\Gamma_0 = 32 \pm 10.6, \Gamma_1 \to 0, A = 51.9 \pm 9.0, B = 27.8 \pm 7.3$ with magnetic exchange couplings as listed in the main text.

To illustrate how neutron scattering can probe spin waves in two high symmetry directions of twinned samples, we note that in the AF orthorhombic phase, the static AF order occurs at the AF wave vector $\boldsymbol{Q}$ = (1, 0, L = 1,3,5…) rlu and the AF Bragg peak is NOT allowed at $\boldsymbol{Q}$ = (0, 1, L = 1,3,5…) rlu (Ref. 33). Therefore, spin waves originating from each of the twin domains of the $BaFe_2As_2$ in the AF orthorhombic phase will not overlap until they are near the zone boundary. Figure A1 shows spin wave intensity

calculations as a function of energy for twinned and detwinned $BaFe_2As_2$ using identical parameters as discussed in the text. For most spin wave energies of interest, the effect of twinning is simply to have two single domain excitations rotated by 90 degrees (Figs. A1a-d).

Figure A2 shows our calculated dispersion curves in the case of twinned and single domain samples. As one can see from the spectra, the effect of twinning will only become important near the top of the band with a very small intensity contribution. Figure A3 shows constant energy cuts of the spin wave dispersions along two high symmetry directions as a function of increasing energy and our model fit using the Heisenberg Hamiltonian with anisotropic damping as discussed in the text. The solid lines are model fits to the data after convolving the cross section with the instrumental resolution. Both the intensity and line-width of the excitations are considered in the model.

To demonstrate that the $J_{1a} = J_{1b}$ Heisenberg Hamiltonian cannot describe the high-energy zone boundary spin wave data, we show in Fig. A4 the best fit of the low-energy spin wave data with $SJ_{1a} = SJ_{1b} = 18.3 \pm 1.4,\ SJ_2 = 28.7 \pm 0.5, SJ_c = 1.85,\ SJ_s =$ 0.084 meV, and isotropic spin wave damping $\Gamma = 21 \pm 2$ (Ref. 7). We have calculated both the detwinned and twinned case. It is clear that the line-shape and intensity of the high-energy spin waves for this model disagree with the observation in Fig. 2. Fig. A5 and Fig. A6 show the output from the best fit of the $SJ_{1a} = SJ_{1b}$ model to the spin wave

data. As one can see, the fit describes the low-energy spin wave data fairly well but fails to account for the high-energy zone boundary spin wave data (ref. 34).

Finally, to illustrate the dramatic difference in high-energy spin waves between $BaFe_2As_2$ and $CaFe_2As_2$, we show in Fig. A7 constant-energy images of the spin waves for these two materials. Since the AF structure, twinning, and lattice structure of $BaFe_2As_2$ and $CaFe_2As_2$ are identical, one would expect that the effective AF exchange couplings in these materials should be similar. Inspection of Fig. A7 reveals that spin waves of $BaFe_2As_2$ at $E = 144 \pm 15$ meV no longer form a ring centered around the AF ordering wave vector as in the case of $CaFe_2As_2$. The only way to interpret these data is to assume that spin waves along the (1,0) direction are heavily damped and no longer observable for $BaFe_2As_2$

Although we have discussed the microscopic origin of the electronic anisotropy as a spin nematic phase, the origin of the anisotropic damping can be understood in terms of excitations across the Fermi surface. Recent RPA calculations (Ref. 27) of the particle-hole excitation spectrum reveal that these excitations are also anisotropic, however they are suppressed below 200 meV due to a partially opened gap in the density of states at the Fermi energy. In $BaFe_2As_2$ we found experimentally that the anisotropic damping switches on around 100 meV. This would imply that the 200 meV pseudogap is overestimated by about a factor of 2 in their study. Thus, by renormalizing the particle-hole excitation spectrum to this experimental threshold value and taking the damping intensity to be in correspondence with this particle-hole spectrum, it may be possible to

replace our phenomenological damping function with a more theoretically sound counterpart. To test this relationship, the energy of the RPA calculation was scaled by ~0.6 and the spin-wave band intensity was determined along the *H* and *K* directions. Upon direct comparison with our data we find that both the dispersion and anisotropic intensity are in excellent agreement with theory (see Fig. A8). Hence, this implies that the pseudogap in the density of states strongly influences the observed spin-wave scattering. Indeed, in $CaFe_2As_2$ a similar threshold value of 100 meV was originally determined but with strong Q-isotropic damping $\Gamma(E)$ appearing above this energy (Ref. 8) leading the authors to conclude that the pseudogap may have provided a low energy window for the formation of local moment excitations that can be well described by the Heisenberg model, but that above this value the excitations quickly evolved into a Stoner picture. Later studies on $CaFe_2As_2$ revealed that well defined spin-waves could still be observed out to the zone boundary, thereby ruling out a quick evolution into a Stoner continuum above 100 meV (Ref. 7). Nonetheless, both studies support an increase in itinerancy as a function of energy with our $BaFe_2A_2$ study, consistent with the idea that the pseudogap drives a transition from local moment to itinerant physics, but with particle-hole excitations favoring the AF direction. Since no damping anisotropy was observed in $CaFe_2As_2$, it is possible that the pseudogap is larger than the spin-wave bandwidth in this system. As a result only $\boldsymbol{Q}$-isotropic damping from electron-magnon interactions are visible.

References:

1. I. I. Mazin, *Nature* **464**, 183 (2010).
2. K. Kuroki, S. Onari, R. Arita, H. Usui, Y. Tanaka, H. Kontani, and H. Aoki, *Phys. Rev. Lett*. **101**, 087004 (2008).
3. A. V. Chubukov, *Physica C* **469**, 640 (2009).
4. F. Wang, H. Zhai, Y. Ran, A. Vishwanath, and D.-H. Lee, *Phys. Rev. Lett*. **102**, 047005 (2009).
5. C. de la Cruz, Q. Huang, J. W. Lynn, J. Y. Li, W. Ratcliff, J. L. Zarestky, H. A. Mook, G. F. Chen, J. L. Juo, N. L. Wang, and P. C. Dai, *Nature* **453**, 899 (2008).
6. Q. Huang, Y. Qku, W. Bao, M. A. Green, J. W. Lynn, Y. C. Gasparovic, T. Wu, G. Wu, and X. H. Chen, *Phys. Rev. Lett.* **101**, 257003 (2008).
7. J. Zhao, D. T. Adroja, D. X. Yao, R. Bewley, S. Li, X. F. Wang, G. Wu, X. H. Chen, and P. C. Dai, *Nat. Phys*. **5**, 555 (2009).
8. S. O. Diallo, V. P. Antropov, T. G. Perring, C. Broholm, J. J. Pulikkotil, N. Ni, S. L. Bud'ko, P. C. Canfield, A. Kreyssig, A. I. Goldman, R. J. McQueeney, *Phys. Rev. Lett*. **102**, 187206 (2009).
9. J. H. Dai, Q. Si, J. X. Zhu, and E. Abrahams, *PNAS* **106**, 4118 (2009).
10. C. Fang, H. Yao, W. F. Tsai, J. P. Hu, and S. A. Kivelson, *Phys. Rev. B* **77**, 224509 (2008).
11. C. K. Xu, M. Muller, and S. Sachdev, *Phys. Rev. B* **78**, 020501(R) (2008).

12. E. Fradkin, S. A. Kivelson, M. J. Lawler, J. P. Eisenstein, A. P. Mackenzie, *Annu. Rev. Condens. Matter Phys*. **1**, 153 (2010).

13. T.-M. Chuang, M. P. Allan, J. H. Lee, Y. Xie, N. Ni, S. L. Bud'ko, G. S. Boebinger, P. C. Canfield, and J. C. Davis, *Science* **327**, 181 (2010).

14. J.-H. Chu, J. G. Analytis, K. De Greve, P. L. McMahon, J. Islam, Y. Yomatomo, and I. R. Fisher, *Science* **329**, 824 (2010).

15. M. A. Tanatar, E. C. Blomberg, A. Kreyssig, M. G. Kim, N. Ni, A. Thaler, S. L. Bud'ko, P. C. Canfield, A. I. Goldman, I. I. Mazin, and R. Prozorov, *Phys. Rev. B* **81**, 184508 (2010).

16. A. Dusza, A. Lucarelli, F. Pfuner, J.-H., Chu, I. R. Fisher, and L. Deglorgi, *EPL* **93**, 37002 (2011)..

17. M. Yi *et al*., *PNAS* **108**, 6878 (2011).

18. Z. P. Yin & W. E. Pickett, *Phys. Rev. B* **81**, 174534 (2010).

19. T. Yildirim, *Physica C* **469**, 425 (2009).

20. I. I. Mazin & M. D. Johannes, *Nat. Phys*. **5**, 141 (2009).

21. C. -C. Lee, W.-G. Yin, & W. Ku, *Phys. Rev. Lett*. **103**, 267001 (2009).

22. F. Krüger, S. Kumar, J. Zaanen, and J. van den Brink, *Phys. Rev. B* **79**, 054504 (2009).

23. W. C. Lv, F. Krüger, & P. Phillips, *Phys. Rev. B* **82**, 045125 (2010).

24. R. Applegate, J. Oitmaa, & R. R. P. Singh, *Phys. Rev. B* **81**, 024505 (2010).

25. R. A. Ewings, T. G. Perring, R. I. Bewley, T. Guidi, M. J. Pitcher, D. R. Parker, S. J. Clarke, and A. T. Boothroyd, *Phys. Rev. B* **78**, 220501(R) (2008).

26. K. Matan, R. Morinaga, K. Lida, and T. J. Sato, *Phys. Rev. B* **79**, 054526 (2009).

27. E. Kaneshita and T. Tohyama, *Phys. Rev. B* **82**, 094441 (2010).

28. S. O. Diallo, D. K. Pratt, R. M. Fernandes, W. Tian, J. L. Zarestky, M. Lumsden, T. G. Perring, C. L. Broholm, N. Ni, S. L. Bud'ko, P. C. Canfield, H.-F. Li, D. Vaknin, A. Kreyssig, A. I. Goldman, and R. J. McQueeney, *Phys. Rev. B* **81**, 214407 (2010).

29. E. Bascones, M. J. Calderon, and B. Valenzuela, *Phys. Rev. Lett*. **104**, 227201 (2010).

30. O. Lipscombe, L. W. Harriger, P. G. Freeman, M. Enderie, C. L. Zhang, M. Y. Wang, T. Egami, J. P. Hu, M. R. Norman, and P. C. Dai, *Phys. Rev. B* **82**, 064515 (2010).

31. M. A. Tanatar, J.-Ph. Reid, H. Shakeripour, X. G. Luo, N. Doiron-Leyraud, N. Ni, S. L. Bud'ko, P. C. Canfield, R. Prozorov, L. Taillefer, *Phys. Rev. Lett.* **104**, 067002 (2010).

32. R. A. Ewings, T. G. Perring, J. Gillett, S. D. Das, S. E. Sebastian, A. E. Taylor, T. Guidi, and A. T. Boothroyd, *Phys. Rev. B* **83**, 214519 (2011).

33. J. Zhao, W. Ratcliff, J. W. Lynn, G. F. Chen, J. L. Luo, N. L. Wang, J. P. Hu, and P. C. Dai, *Phys*. *Rev. B* **78**, 140504(R) (2008).

34. T. G. Perring, D. T. Adroja, G. Chaboussant, G. Aeppli, T. Kimura, and Y. Tokura, *Phys. Rev. Lett*. **87**, 217201 (2001); Tobyfit program available at http://tobyfit.isis.rl.ac.uk/Main_Page.

1.

Figure 1 a) The AF Fe spin ordering in $BaFe_2As_2$ with the magnetic exchange couplings J_{1a}, J_{1b}, J_2 along different directions. b) Temperature dependence of the resistivity in detwinned $BaFe_2As_2$ (from [14]). The inset is a plot of the resistivity for the twinned sample used in our neutron measurements, with the blue points corresponding to $T = 7, 125, 150$ K. c) Color plots describing qualitatively how the spin wave scattering evolves from $\boldsymbol{Q}$ = (1, 0) to (1, 1) as a function of energy using an anisotropic damping Γ. The solid black contours are an overlay of the same model but with no damping. The exchange couplings used in both plots are from best fits of the data. d) Color plots of the anisotropic damping Γ, which is much stronger along the *H*-direction than along the *K*-direction. e) Spin wave dispersion along the (1, *K*) direction as determined by energy and $\boldsymbol{Q}$-cuts of the raw data in Fig. 2 below and above T_N. The solid line is a Heisenberg model calculation using anisotropic exchange couplings $SJ_{1a} = 59.2 \pm 2.0$, $SJ_{1b} = -9.2 \pm 1.2$, $SJ_2 = 13.6 \pm 1.0$, $SJ_c = 1.8 \pm 0.3$ meV determined by fitting the full cross-section. The dotted line is a Heisenberg model calculation assuming isotropic exchange coupling $SJ_{1a} = SJ_{1b} = 18.3 \pm 1.4$, $SJ_2 = 28.7 \pm 0.5$, and $SJ_c = 1.8$ meV. f) Dispersion along the (*H*, 0) direction; data points beyond *H* = 1.4 could not be reliably obtained due to strong damping at higher energies. The red shading stresses how the damping grows as a function of *H*. Error bars are systematic and represent the difference between $\boldsymbol{Q}$ and *E* cut dispersion points. The statistical error of the $\boldsymbol{Q}$ and *E* cuts are much smaller.

Figure 2 Wave vector dependence of the spin waves for energy transfers of a) $E = 26 \pm 10$ meV [$E_i = 450$ meV and $Q = (H, K, 1)$]; b) $E = 81 \pm 10$ meV [$E_i = 450$ meV and $Q = (H, K, 3)$]; c) $E = 113 \pm 10$ meV [$E_i = 450$ meV and $Q = (H, K, 5)$]; d) $E = 157 \pm 10$ meV [$E_i = 600$ meV and $Q = (H, K, 5)$]; e) $E = 214 \pm 10$ meV [$E_i = 600$ meV and $Q = (H, K, 7)$]; f) The projection of the spin waves on the energy transfer axis and (1,*K*) direction (with integration of *H* from 0.8 to 1.2 rlu) after subtracting the background integrated from $1.8 < H < 2.2$ and from $-0.25 < K < 0.25$ with $E_i = 450$ meV. The color bar scales represent the absolute spin wave intensity in units of mbarn/sr/meV/f.u. and the dashed boxes indicate zone boundaries. The missing low-energy data in f) is due to imperfect data subtraction. g-l) Model calculation of identical slices as in a-f) using anisotropic exchange couplings from best fits and convolved with the instrumental resolution.

Figure 3 Spin waves of $E = 50 \pm 10$ meV a-c); $E = 75 \pm 10$ meV d-f); $E = 125 \pm 10$ meV g-i); and $E = 150 \pm 10$ meV j-l) for temperatures of $T = 7$, 125, and 150 K. The dashed curves show fixed reciprocal space sizes at different temperatures.

Figure 4 The blue diamonds in a-d) are constant-$\boldsymbol{Q}$ cuts at $\boldsymbol{Q}$ = (1,0.05), (1,0.2), (1,0.35), and (1,0.5), respectively, at $T = 7$ K. The green squares and red circles in a-d) are identical constant-$\boldsymbol{Q}$ cuts at $T = 125$, and 150 K, respectively. The dashed lines indicate paramagnetic scattering at low energies centered at $E = 0$ meV. e,f) $\boldsymbol{Q}$-dependence of the spin wave excitations below and above T_N obtained through constant-*E* cuts at $E = 19 \pm 5$ and 128 ± 5 meV. The solid lines in a-f) are fits to the anisotropic spin-wave model

discussed in the text and the horizontal bars represent the instrumental energy (E)/wave vector ($\boldsymbol{Q}$) resolution. g) Energy dependence of the dynamic spin-spin correlation lengths below and above T_N obtained by Fourier transform of constant-E cuts similar to e,f).

Fig. A1 The effect of twinning on spin waves of $BaFe_2As_2$ with L = 1,3,5,7.

Fig. A2 The effect of twinning on the dispersion curves of $BaFe_2As_2$.

Fig. A3 Constant energy cuts of the spin wave excitations at 7 K and our model fits to the data using an anisotropic Heisenberg Hamiltonian convolved with the instrumental resolution. The solid lines are the output from the Toby fit program[ii] using fitting parameters as discussed in the text of the paper.

Fig. A4 The effect of twinning on spin waves of $BaFe_2As_2$ with isotropic J_{1a} and J_{1b} and L = 1,3,5,7.

Fig. A5 The effect of twinning on the dispersion curves of $BaFe_2As_2$ in the J_{1a} and J_{1b} model.

Fig. A6 Constant energy cuts of the spin wave excitations at 7 K and the $J_{1a} = J_{1b}$ model fits to the data using an anisotropic Heisenberg Hamiltonian convolved with the instrumental resolution. The solid lines are the output from the Toby fit program[ii] using fitting parameters as discussed in the supplementary material. While this model fits the

low-energy spin wave data reasonably well, it completely fails to describe the data for spin wave energies above 100 meV.

Fig. A7 Constant energy cuts of the spin wave excitations at 7 K for $BaFe_2As_2$ and $CaFe_2As_2$ in absolute units within the first Brillouin zone. The data for $CaFe_2As_2$ are from Ref. 7.

Fig. A8 Comparison of a normalized RPA calculation from [27] and our data. Given the normalization correction, RPA appears to fit the data.

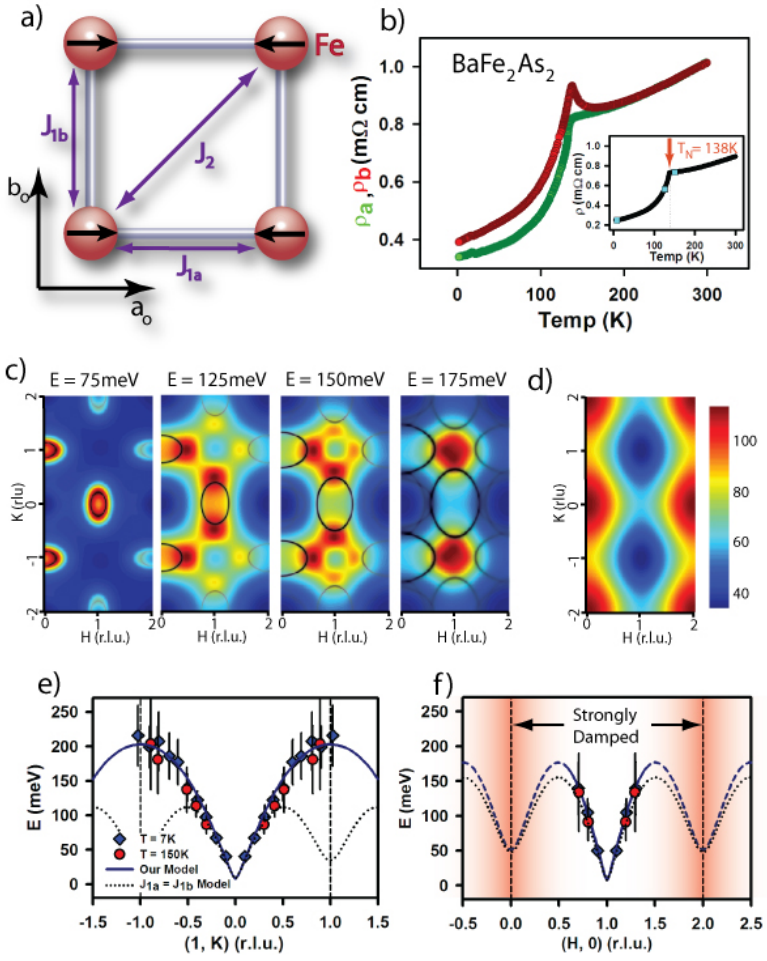
a)
Fe
J_{1b}
J_2
J_{1a}
b_o
a_o
b)
$BaFe_2As_2$
$\rho a, \rho b$ (mΩ cm)
T_N= 138K
Temp (K)
c)
E = 75meV
E = 125meV
E = 150meV
E = 175meV
K (rlu)
H (r.l.u.)
d)
e)
E (meV)
T = 7K
T = 150K
Our Model
$J_{1a} = J_{1b}$ Model
(1, K) (r.l.u.)
f)
Strongly
Damped
(H, 0) (r.l.u.)

Fig. 1

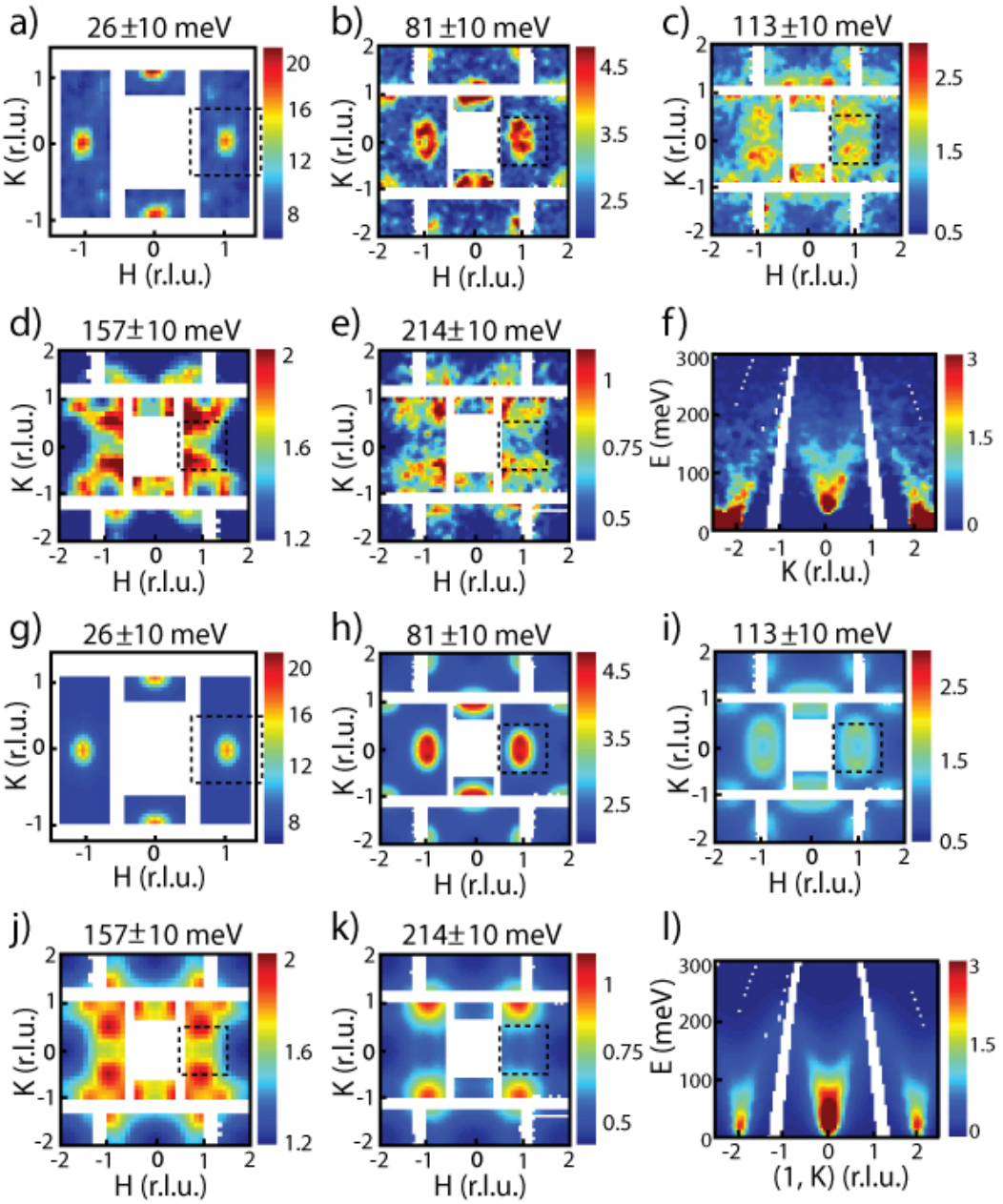
a)
26±10 meV
b)
81±10 meV
c)
113±10 meV
d)
157±10 meV
e)
214±10 meV
f)
g)
26±10 meV
h)
81±10 meV
i)
113±10 meV
j)
157±10 meV
k)
214±10 meV
l)
K (r.l.u.)
H (r.l.u.)
E (meV)
(1, K) (r.l.u.)

Fig. 2

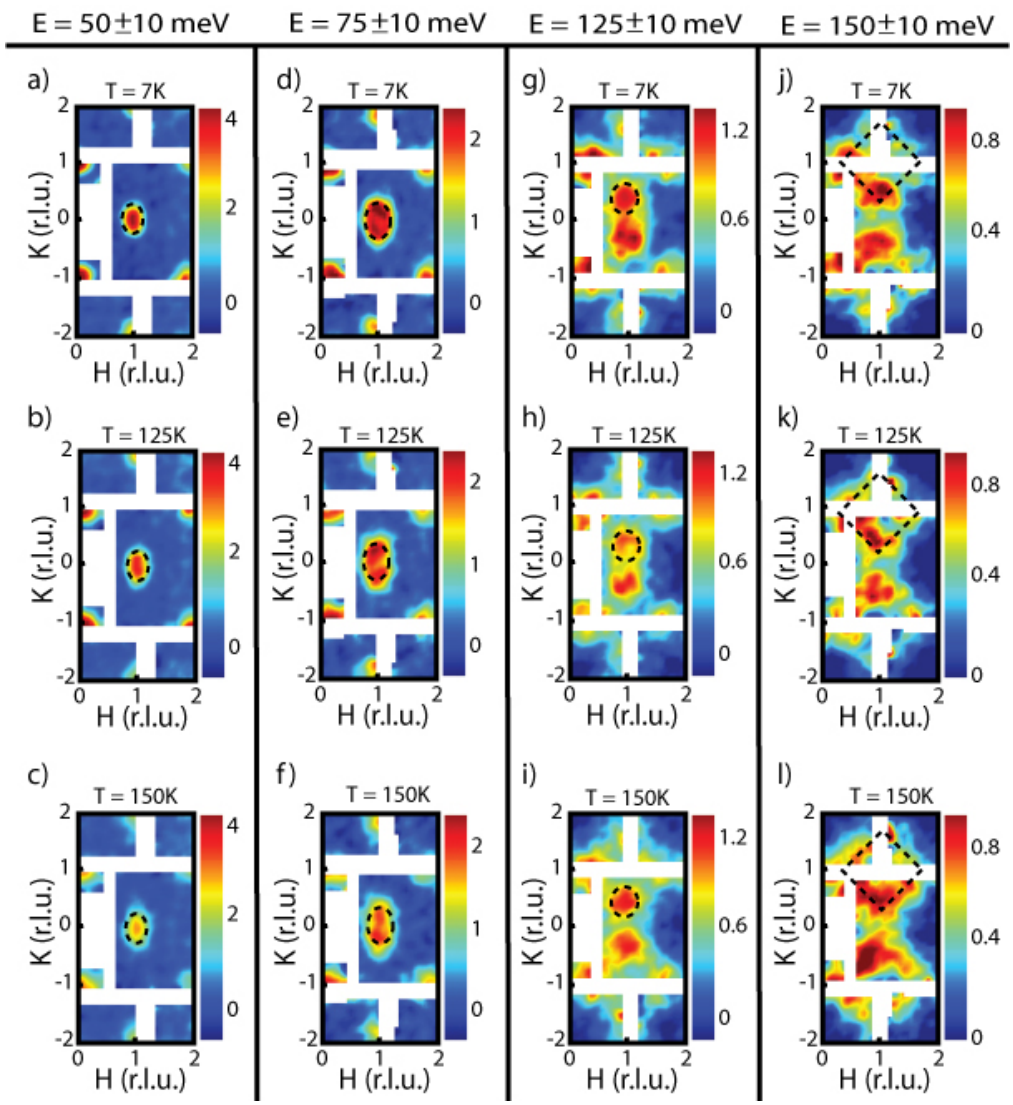
E = 50±10 meV
E = 75±10 meV
E = 125±10 meV
E = 150±10 meV
a)
b)
c)
d)
e)
f)
g)
h)
i)
j)
k)
l)
T = 7K
T = 125K
T = 150K
K (r.l.u.)
H (r.l.u.)

Fig. 3

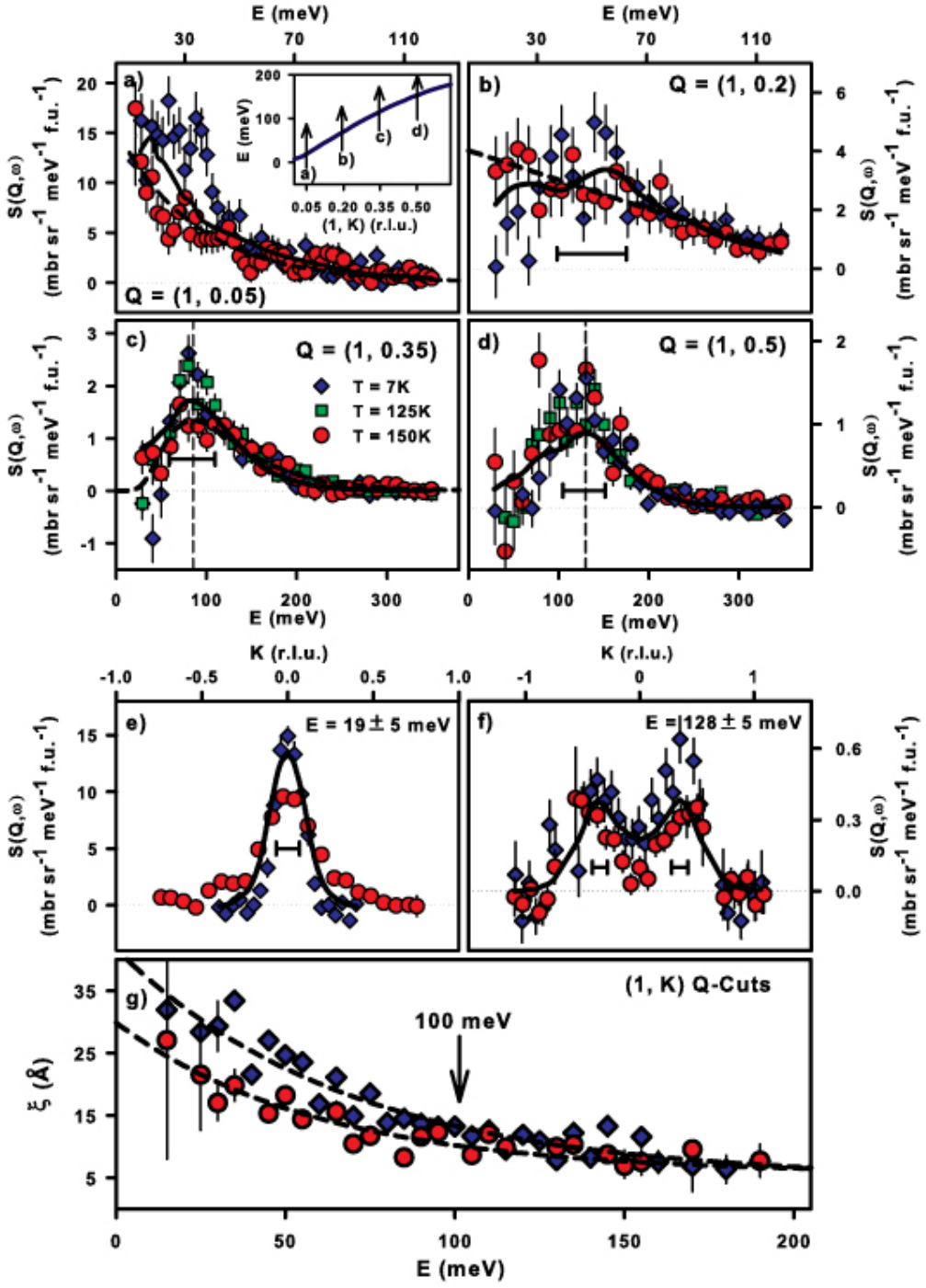
E (meV)
a)
Q = (1, 0.05)
b)
Q = (1, 0.2)
c)
Q = (1, 0.35)
T = 7K
T = 125K
T = 150K
d)
Q = (1, 0.5)
S(Q,ω) (mbr sr-1 meV-1 f.u.-1)
E (meV) (1, K) (r.l.u.)
K (r.l.u.)
e)
E = 19 ± 5 meV
f)
E = 128 ± 5 meV
g)
(1, K) Q-Cuts
100 meV
ξ (Å)

Fig. 4

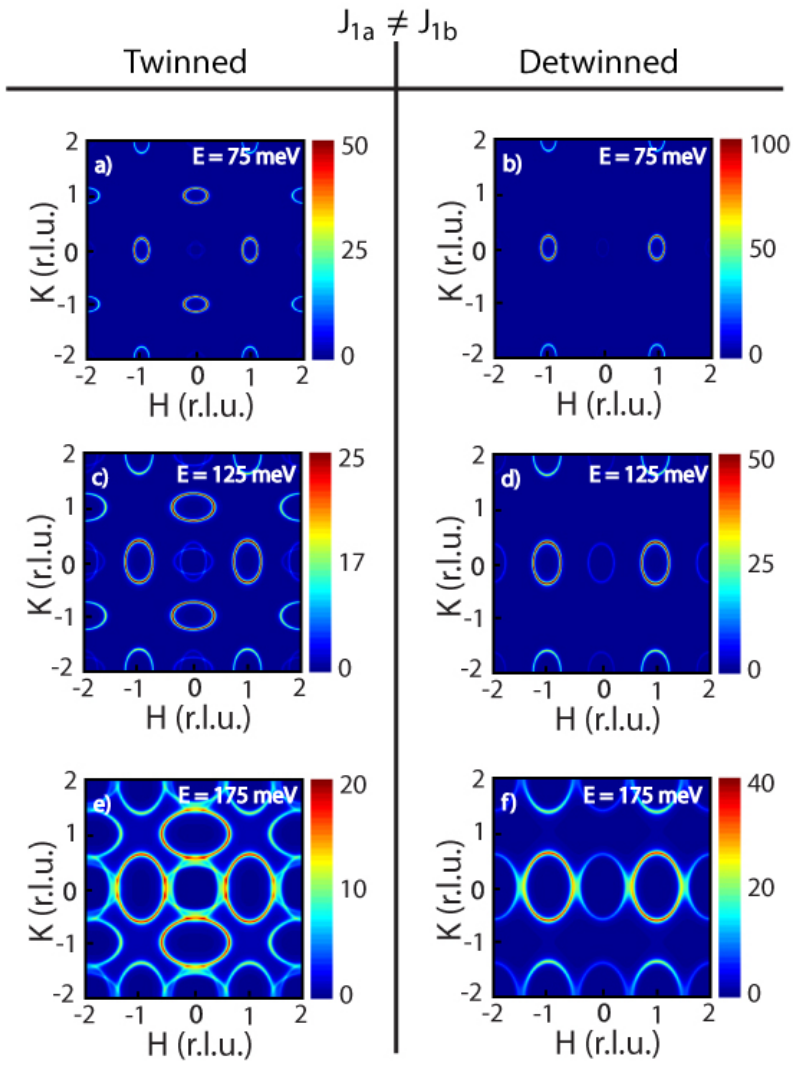
$J_{1a} \neq J_{1b}$
Twinned
Detwinned
a)
E = 75 meV
b)
E = 75 meV
c)
E = 125 meV
d)
E = 125 meV
e)
E = 175 meV
f)
E = 175 meV
K (r.l.u.)
H (r.l.u.)
50
25
0
100
50
0
25
17
0
50
25
0
20
10
0
40
20
0

Fig. A1

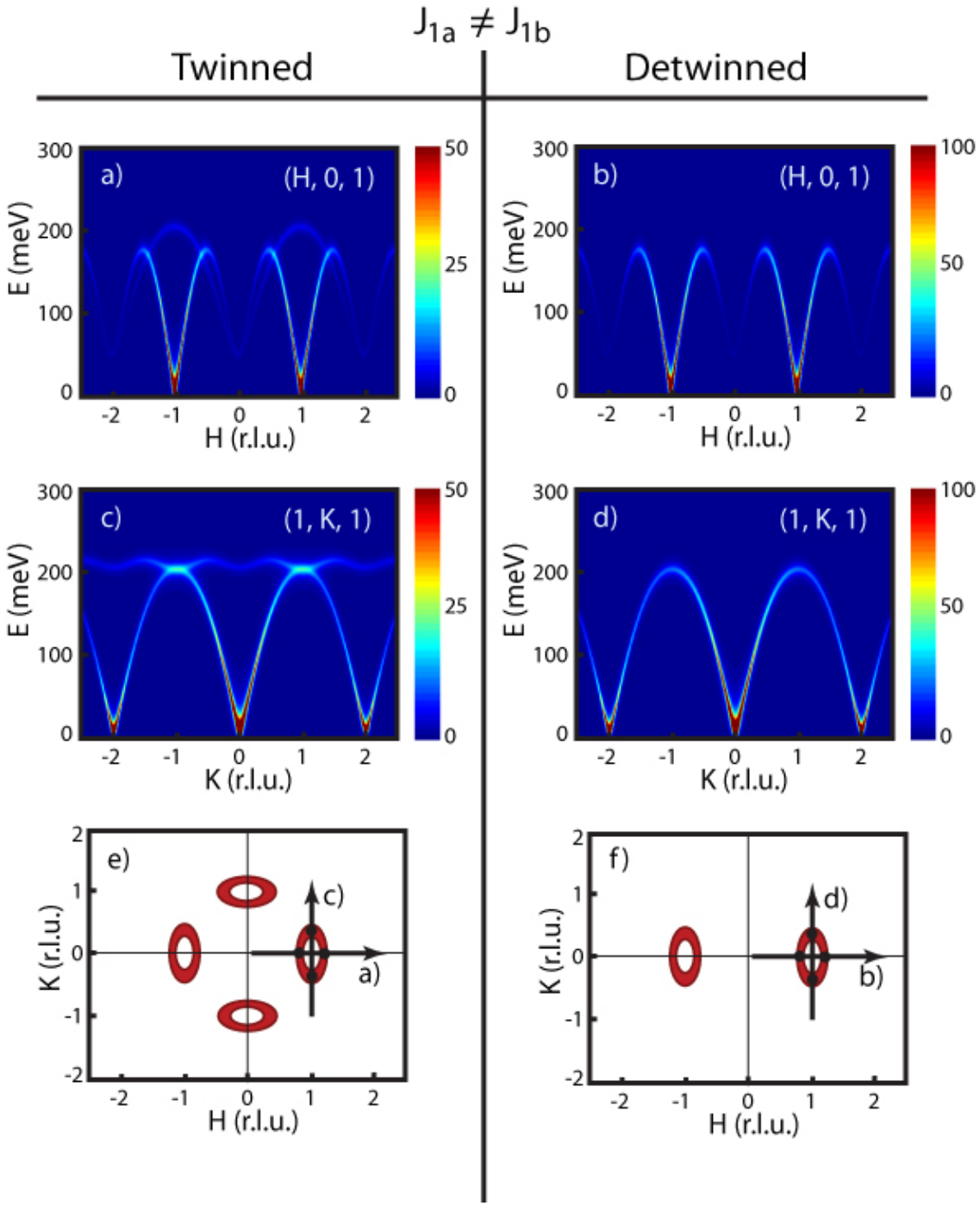
$J_{1a} \neq J_{1b}$
Twinned
Detwinned
a)
(H, 0, 1)
b)
(H, 0, 1)
c)
(1, K, 1)
d)
(1, K, 1)
E (meV)
H (r.l.u.)
K (r.l.u.)
e)
f)
a)
b)
c)
d)

Fig. A2

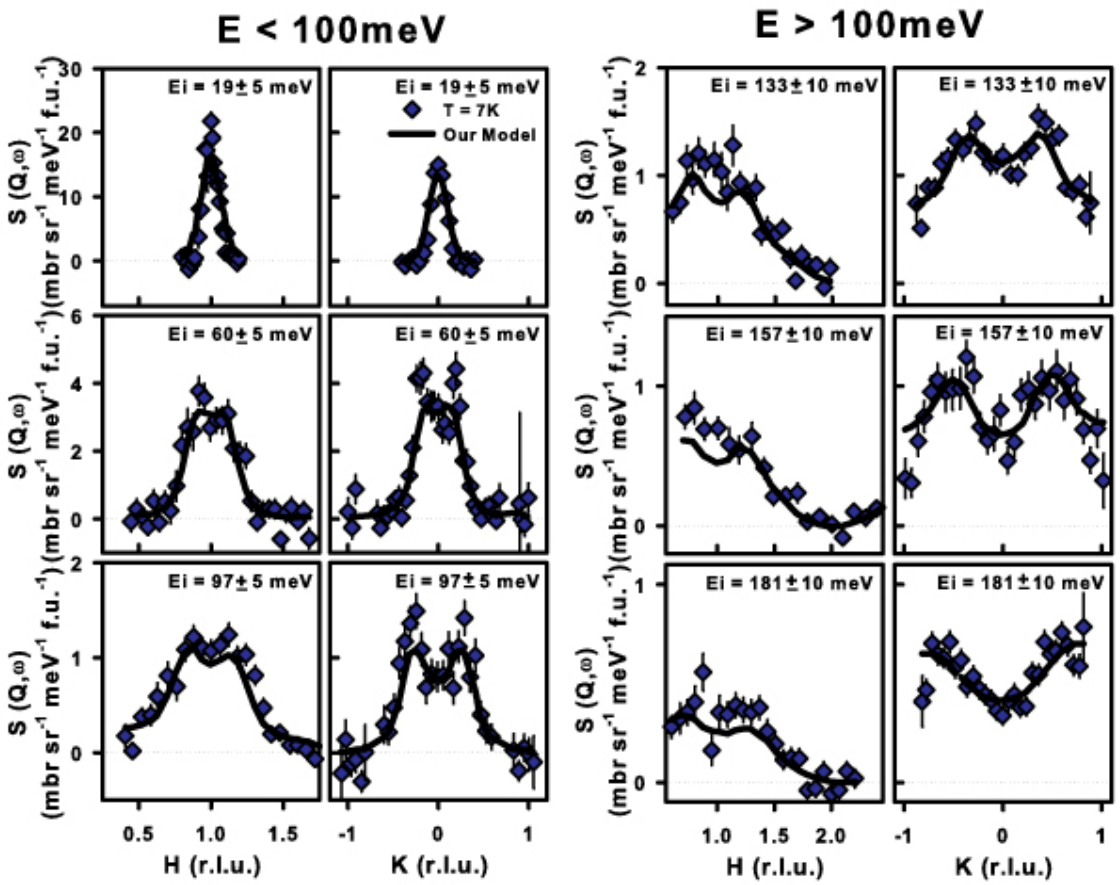
E < 100meV
E > 100meV
Ei = 19±5 meV
Ei = 19±5 meV
T = 7K
Our Model
Ei = 60±5 meV
Ei = 60±5 meV
Ei = 97±5 meV
Ei = 97±5 meV
Ei = 133±10 meV
Ei = 133±10 meV
Ei = 157±10 meV
Ei = 157±10 meV
Ei = 181±10 meV
Ei = 181±10 meV
S (Q,ω) (mbr sr-1 meV-1 f.u.-1)
H (r.l.u.)
K (r.l.u.)

Fig. A3

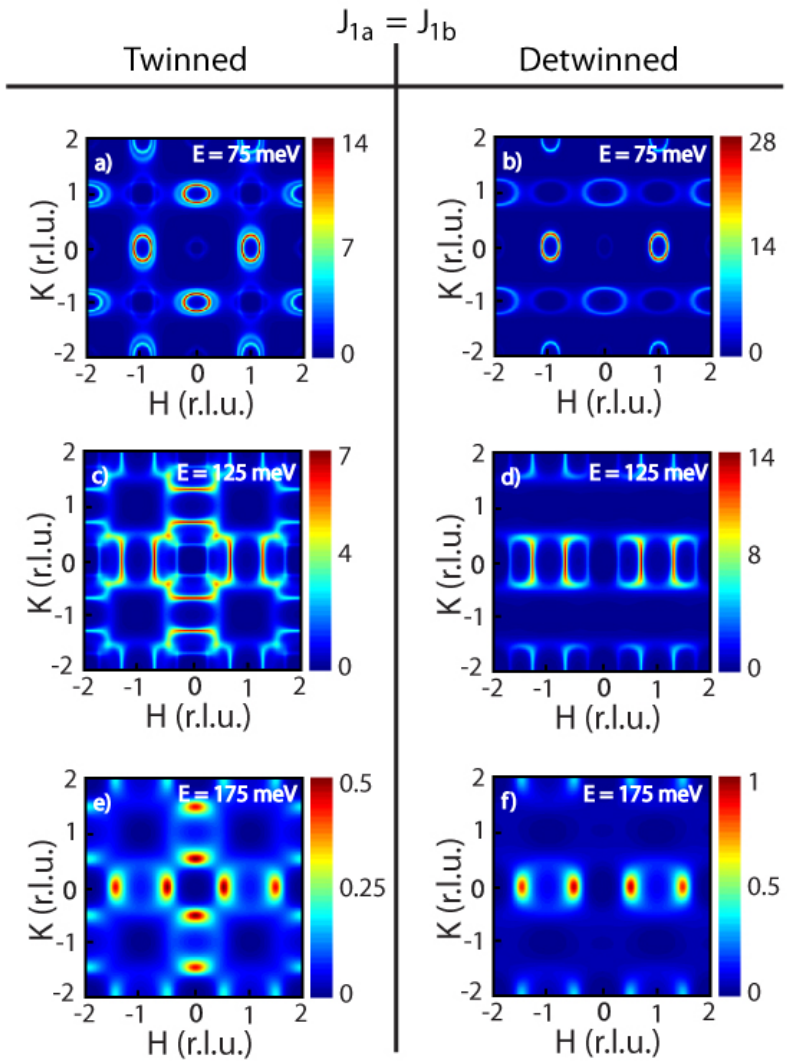
$J_{1a} = J_{1b}$
Twinned
Detwinned
a) E = 75 meV
b) E = 75 meV
c) E = 125 meV
d) E = 125 meV
e) E = 175 meV
f) E = 175 meV
K (r.l.u.)
H (r.l.u.)
14
7
0
28
4
8
0.5
0.25
1

Fig. A4

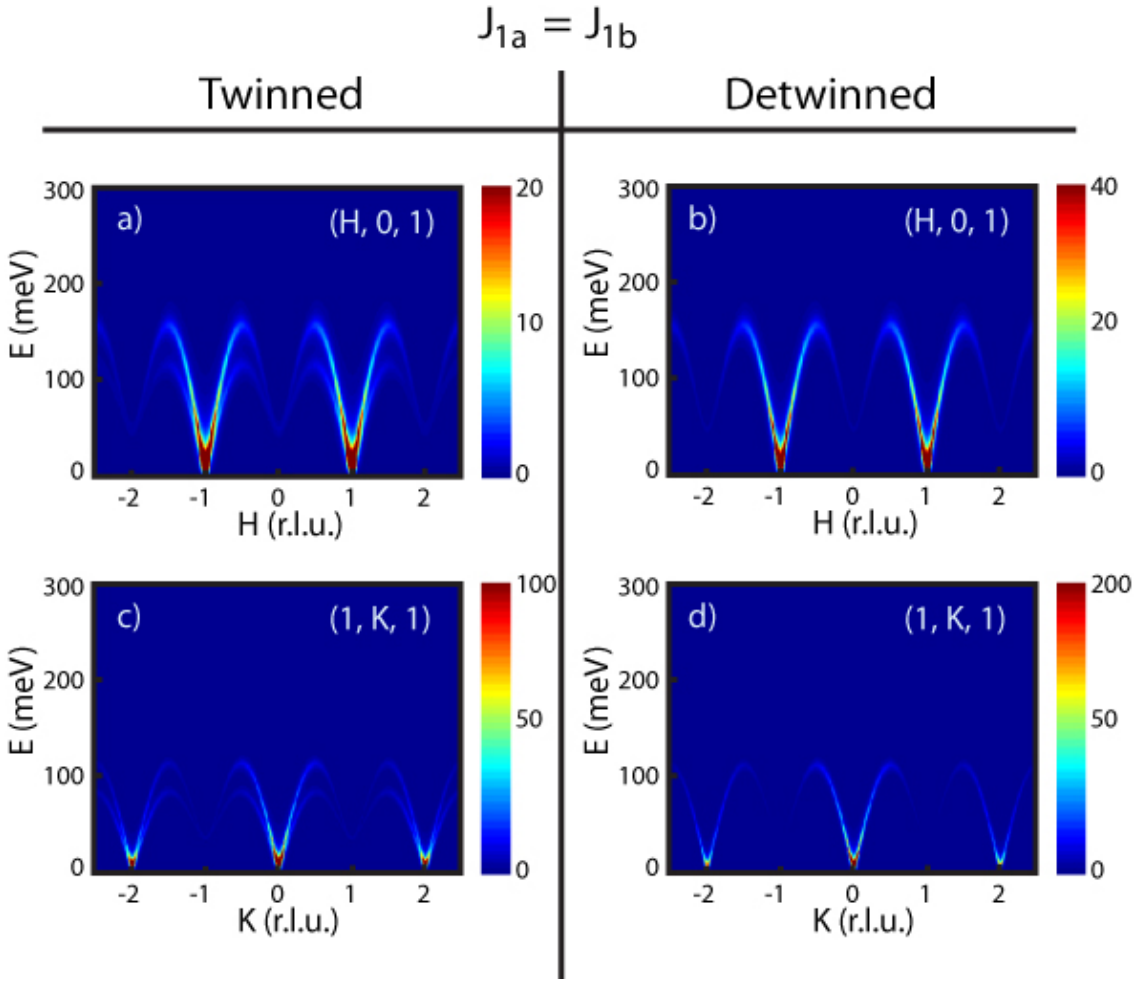
$J_{1a} = J_{1b}$
Twinned
Detwinned
a)
(H, 0, 1)
b)
(H, 0, 1)
c)
(1, K, 1)
d)
(1, K, 1)
E (meV)
H (r.l.u.)
K (r.l.u.)
300
200
100
0
-2
-1
0
1
2
20
10
40
100
50
200

Fig. A5

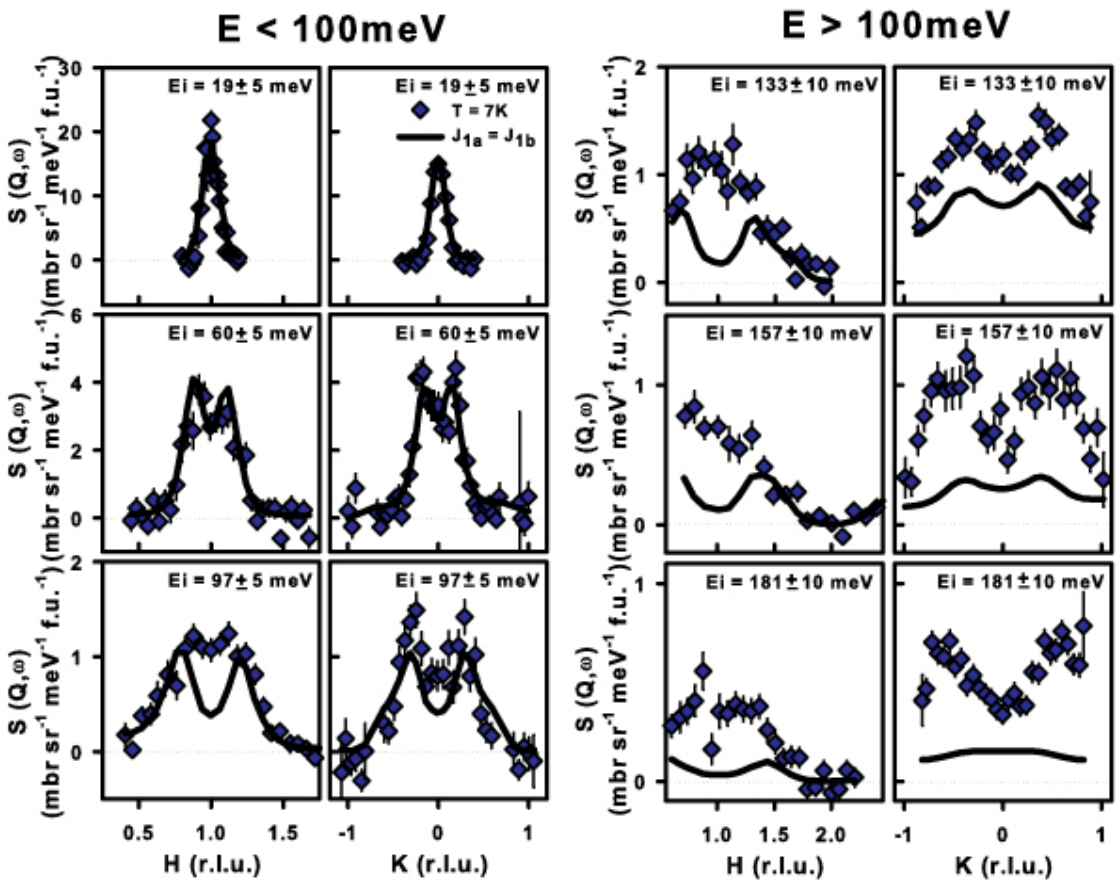
E < 100meV
E > 100meV
Ei = 19±5 meV
Ei = 19±5 meV
T = 7K
J1a = J1b
Ei = 60±5 meV
Ei = 60±5 meV
Ei = 97±5 meV
Ei = 97±5 meV
Ei = 133±10 meV
Ei = 133±10 meV
Ei = 157±10 meV
Ei = 157±10 meV
Ei = 181±10 meV
Ei = 181±10 meV
S (Q,ω) (mbr sr-1 meV-1 f.u.-1)
H (r.l.u.)
K (r.l.u.)

Fig. A6

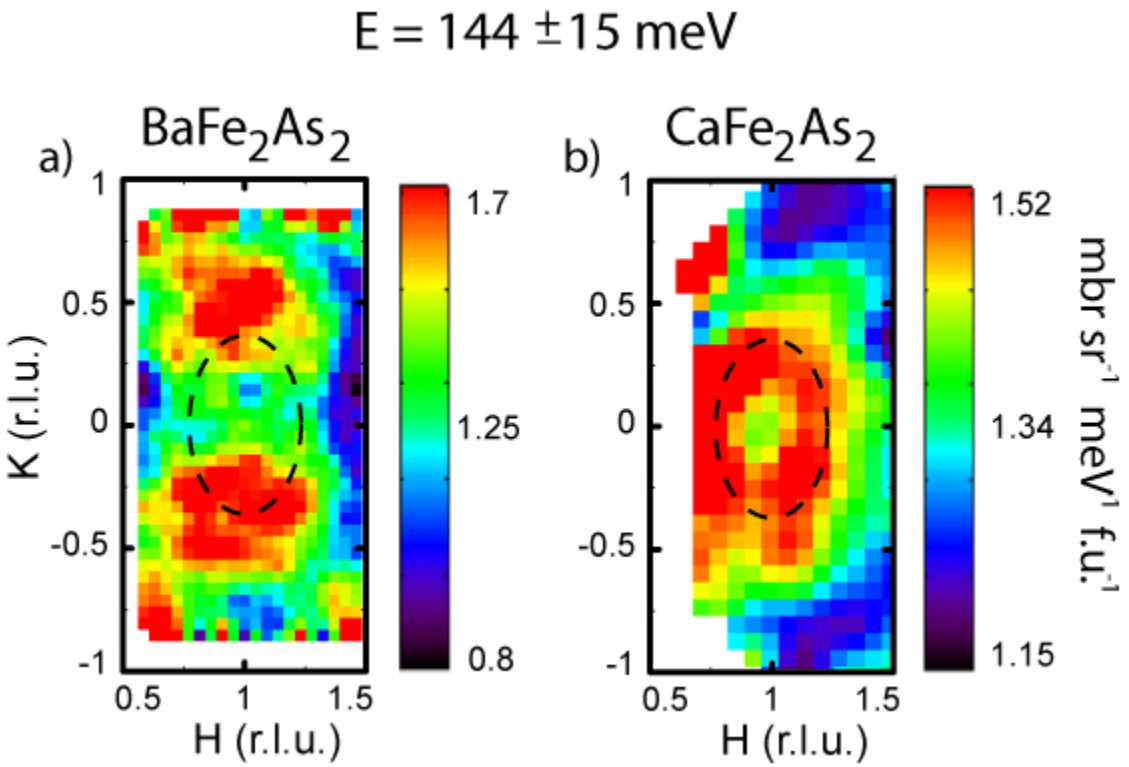
E = 144 ±15 meV
a)
BaFe2As2
b)
CaFe2As2
K (r.l.u.)
H (r.l.u.)
H (r.l.u.)
1
0.5
0
-0.5
-1
0.5
1
1.5
1.7
1.25
0.8
1.52
1.34
1.15
mbr sr-1 meV-1 f.u.-1

Fig. A7

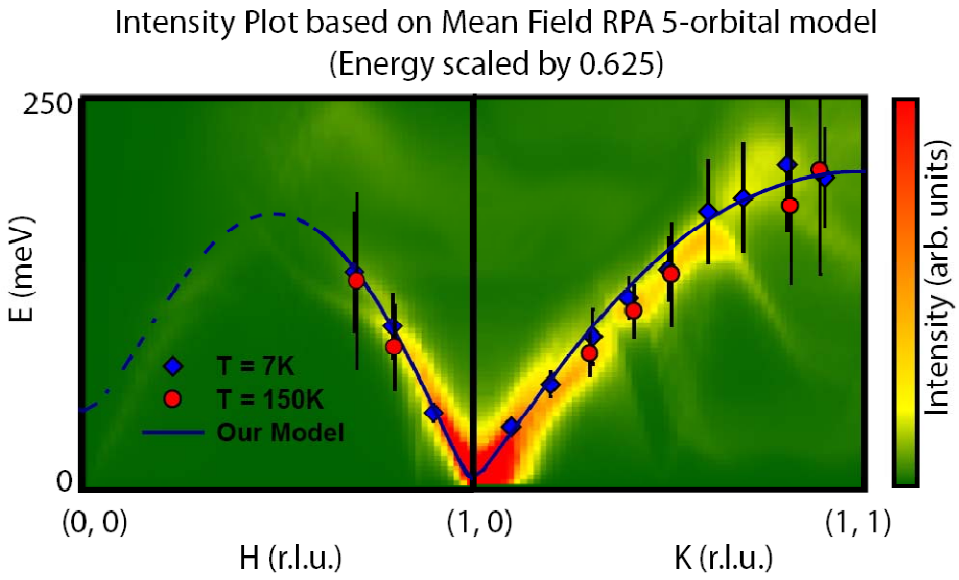
Intensity Plot based on Mean Field RPA 5-orbital model
(Energy scaled by 0.625)
250
0
E (meV)
T = 7K
T = 150K
Our Model
(0, 0)
(1, 0)
(1, 1)
H (r.l.u.)
K (r.l.u.)
Intensity (arb. units)

Fig. A8